Experimental and Numerical Study of The Shock-Accelerated Elliptic Heavy Gas Cylinders

Jing S. Bai, Li Y. Zou, Tao Wang, Kun Liu, Wen B. Huang, Jin H. Liu, Ping Li, Duo W. Tan, and Cang L. Liu

Abstract—We studied the evolution of elliptic heavy SF_6 gas cylinder surrounded by air when accelerated by a planar Mach 1.25 shock. A multiple dynamics imaging technology has been used to obtain one image of the experimental initial conditions and five images of the time evolution of elliptic cylinder. We compared the width and height of the circular and two kinds of elliptic gas cylinders, and analyzed the vortex strength of the elliptic ones. Simulations are in very good agreement with the experiments, but due to the different initial gas cylinder shapes, a certain difference of the initial density peak and distribution exists between the circular and elliptic gas cylinders, and the latter initial state is more sensitive and more inenarrable.

Keywords—About four key words or phrases in alphabetical order, separated by commas.

I. INTRODUCTION

AN instability induced by a shock wave colliding with an interface between two materials of different density is known as the Richtmyer-Meshkov (RM) instability. Numerous papers [1-4] have investigated the experimental techniques and simulation methods of the shock-accelerated circular heavy gas cylinder. As we all know, initial conditions have a major effect on the development and evolution of the interface instability throughout the process. A one-dimensional (1D) finite interfacial transition layer (ITL) or "diffused cylinder" has been posed by S. Gupta [5]. ITL is an important consideration for the validity of the simulations at late time and an important aspect

J. S. Bai is with Institute of Fluid Physics, China Academy of Engineering Physics, Mianyang, Sichuan 621900, P.R.China (e-mail: bjsong_mail@ 21cn.com).

L. Y. Zou, is with National Key Laboratory of Shock Wave and Detonation Physics (LSD), Institute of Fluid Physics, China Academy of Engineering Physics, Mianyang, Sichuan 621900, P.R.China.

T. Wang is with Institute of Fluid Physics, China Academy of Engineering Physics, Mianyang, Sichuan 621900, P.R.China.

K. Liu is with Institute of Fluid Physics, China Academy of Engineering Physics, Mianyang, Sichuan 621900, P.R.China.

W. B. Huang is with National Key Laboratory of Shock Wave and Detonation Physics (LSD), Institute of Fluid Physics, China Academy of Engineering Physics, Mianyang, Sichuan 621900, P.R.China.

J. H. Liu is with National Key Laboratory of Shock Wave and Detonation Physics (LSD), Institute of Fluid Physics, China Academy of Engineering Physics, Mianyang, Sichuan 621900, P.R.China.

P. Li is with Institute of Fluid Physics, China Academy of Engineering Physics, Mianyang, Sichuan 621900, P.R.China.

D. W. Tang is with National Key Laboratory of Shock Wave and Detonation Physics (LSD), Institute of Fluid Physics, China Academy of Engineering Physics, Mianyang, Sichuan 621900, P.R.China.

C. L. Liu is with National Key Laboratory of Shock Wave and Detonation Physics (LSD), Institute of Fluid Physics, China Academy of Engineering Physics, Mianyang, Sichuan 621900, P.R.China.

for comparison with experimental results. This kind of hydrodynamic RM experiments are mainly realized in shock tubes [6-10]. Many scientists stress the uncertainty in the initial conditions of the interface and the resulting even more uncertainty in the use of experimental data to test numerical schemes. In all known horizontal or vertical shock tube experiments, the initial interfacial conditions are rarely accurately measured [11, 12] but often backward estimated. Recently, the authors investigated the influence of nonuniform flow initial conditions on the interface instability [13] with well-conducted experiments and numerical simulations. Our work illuminated that besides owning the identity of initial interface condition, the initial nonuniform flow would have a significant effect on the RM instability.

This research is motivated by the interest of understanding and controlling the noncircular (elliptic in this paper) gas cylinder shock tube instability experiments and numerical simulations. We arranged three experiments to achieve this goal. The first one was a preparative experiment, in which a shock wave accelerated a circular gas cylinder, while in the two others, the elliptic heavy gas cylinders were driven by shocks in two different vertical directions. The objective of our work is to study the relationship between the circular and elliptic gas cylinders, and construct approximate initial conditions of two-dimensional (2D) diffuse ITL with finite thickness to elliptic ones. In particular we also analyzed the effect of convergence and vortex features of the induced gas cylinders with time under different shock-accelerated directions to the elliptic gas cylinder. To our knowledge this is the first experimental and numerical study with a shock-accelerated elliptic heavy gas cylinder.

II. EXPERIMENTS

The experiments were performed in the National Key Laboratory of Shock Wave and Detonation Physics (LSD) horizontal shock tube which is 5 m long, and 5×5 cm^2 square cross section. It was coupled with a high-speed multiple dynamics imaging technology (the interval between two consecutive frames was 100 μs) which allows a 2D visualization of the interface. Tracer fog was applied to the gas to enhance the light scattered and CCD cameras were used to increase the dynamic range of the images. The interface between light gas (air) and heavy gas (SF_6) was created using a cylindrical contoured nozzle with a diameter of 5.0 mm for the circular gas cylinder, while in the elliptic cases, an elliptic cylindrical contoured nozzle with its major and minor axes of 10.0 mm and 2.5 mm respectively was adopted. The Mach

World Academy of Science, Engineering and Technology
International Journal of Physical and Mathematical Sciences
Vol:5, No:4, 2011

number of the incident shock wave was 1.25 in air. Table I summarizes the properties of air and SF_6 gas in the present experiments at 0.97 atm and 20 ℃. By using the multiple dynamics imaging technology, we obtained one image of the experimental initial conditions and five images of the time evolution of the cylinder two-dimensional diagram from t=200 μs to 600 μs at intervals of 100 μs. Figure 1 shows the typical frames obtained for the three experiments [(a), (c), and (e)] and simulations [(b), (d), and (f)]. The pressure of initial SF_6 gas cylinder is 0.97 atm and the initial spatial distribution of density is difficult to be measured and not known. In our experiments, we mainly estimated the SF_6 gas concentrations at the center of the gas cylinder from the initial images; they are approximate about of 0.87 and 0.71, respectively. Therefore we need to determine the initial distribution of density in the gas cylinder with the help of numerical simulation and experimental results, in order to reproduce the whole experimental process and understand the impacts of different cylinder shapes and different shock-accelerated directions on the development and evolution of cylinders. This work has an important significance on the setting of initial conditions for experimental study of interface instability, analysis of experimental phenomenon and results.
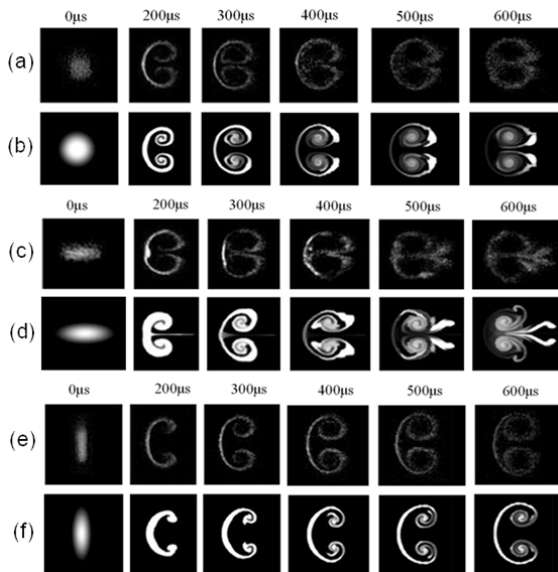

Fig. 1 Multiple dynamics images and numerical simulation results by MVFT at t=200, 300, 400, 500, and 600 μs after shock passage. [The experiments corresponding (a), (c), and (e), and the simulations corresponding (b), (d), and (f)]

III. SIMULATIONS

This paper applies our large eddy simulation code MVFT

TABLE I
PROPERTIES OF AIR AND SF_6 GAS

Gas	Density (kg·m^{-3})	Specific heat ratio	Kinematic viscosity (10^{-6}m^2·s)	Prandtl number	Diffusion coefficient in air (cm^2·s)
Air	1.15	1.40	15.7	0.71	0.204
SF$_6$	5.34	1.09	2.47	0.90	0.097

(multi-viscous flow and turbulent) to numerically simulate the multi-viscosity-fluid and turbulence. MVFT is based on the parabolic method [14], the Vreman [15] subgrid eddy viscosity model, and it solves the Navier-Stokes equations,

$$\begin{cases} \dfrac{\partial \overline{\rho}}{\partial t} + \dfrac{\partial \overline{\rho}\widetilde{u}_j}{\partial x_j} = 0, \\[2mm] \dfrac{\partial \overline{\rho}\widetilde{u}_i}{\partial t} + \dfrac{\partial \overline{\rho}\widetilde{u}_j\widetilde{u}_i}{\partial x_j} + \dfrac{\partial \overline{p}}{\partial x_i} = \dfrac{\partial(\overline{\sigma}_{ij} + \tau_{ij})}{\partial x_j}, \\[2mm] \dfrac{\partial \overline{\rho}\overline{E}}{\partial t} + \dfrac{\partial(\overline{\rho}\widetilde{u}_j\overline{E} + \overline{p}\widetilde{u}_j)}{\partial x_j} = -\dfrac{\partial(\overline{q}_j + Q_j)}{\partial x_j} + \dfrac{\partial(\widetilde{u}_i(\overline{\sigma}_{ij}+\tau_{ij}))}{\partial x_j}, \\[2mm] \dfrac{\partial \overline{Y}^{(s)}}{\partial t} + \widetilde{u}_j \dfrac{\partial \overline{Y}^{(s)}}{\partial x_j} = \dfrac{\partial}{\partial x_j}\left(\widetilde{D}\dfrac{\partial \overline{Y}^{(s)}}{\partial x_j}\right), \ s=1,2,\cdots,N-1. \end{cases} \quad (1)$$

$\overline{\sigma}_{ij} = \mu_l(\partial\widetilde{u}_i/\partial x_j + \partial\widetilde{u}_j/\partial x_i - 2/3\delta_{ij}(\partial\widetilde{u}_k/\partial x_k))$ is the viscous stress tensor, $\tau_{ij} = \rho(\overline{u_iu_j} - \overline{u}_i\overline{u}_j)$ is the subgrid scale (SGS) stress tensor, $\overline{q}_j + Q_j$ is the energy flux of unit time and space, $\overline{q}_j = -\lambda_l\partial\overline{T}/\partial x_j$, $Q_j = -\lambda_t\partial\overline{T}/\partial x_j$, $\lambda_l = \mu_lc_p/p_{\gamma,l}$, $\lambda_t = \mu_tc_p/P_{\gamma,t}$, $\widetilde{D} = \overline{D}_l + D_t$, $S_{c,t} = \mu_t/D_t\overline{\rho}$. μ_l is the fluid viscosity, μ_t is the turbulent viscosity, $\overline{T}$ is the temperature, λ_l is the efficient heat-transfer coefficient, c_p is the specific heat of fluid, $p_{\gamma,l}$ is the Prandtl number, $\overline{D}_l$ is the diffusion coefficient and D_t is the turbulent diffusion coefficient. N is of the kinds of fluids, $\overline{Y}^{(s)}$ is the volume fraction of the sth fluid and satisfies $\sum_1^N \overline{Y}^{(s)} = 1$.

An operator splitting technique is used to decompose the physical problems into three sub-processes in MVFT, i.e., the computations of inviscid flux, viscous flux and heat flux. For the inviscid flux, the three-dimensional problem can be simplified into three 1D problems by dimension-splitting technique. For each 1D problem, we apply two-step Lagrange-Remap algorithm to solve the equations. During one time step, the calculation can be divided into four steps: (i) the piecewise parabolic interpolation of physical quantities, (ii) solving Riemann problems approximately, (iii) marching of Lagrange equations, and (iv) remapping the physical quantities to stationary Euler meshes. More information about the flow equations, algorithms, numerical schemes, and SGS turbulent model, etc., can be obtained in the author's literature [13, 16].

IV. RESULTS AND DISCUSSIONS

For the initial density distribution of the circular SF_6 gas cylinder in the first preparative experiment, numerical simulation is used to approximately describe the interface dissipative transition layer, the same as literature [5]. In the dissipative transition layer, SF_6 gas density is calculated by 1D Gaussian function:

$$\rho(r) = \chi_0\rho_{SF_6}\exp\{-[(r-r_c)^2/\delta^2]\}, \quad (2)$$

World Academy of Science, Engineering and Technology
International Journal of Physical and Mathematical Sciences
Vol:5, No:4, 2011

where $r^2=x^2+y^2$, r_c=0.9 mm, and δ=2.15 mm. χ_0 is the concentration at the center, χ_0=0.87 in the circular case. The initial density image and distribution are plotted in Fig. 2 (a).

However, for the elliptic SF$_6$ gas cylinders, i.e., in the second and third experiments, the initial density distributions are more complex than in the circular case in the numerical simulations. How to determine the density distributions of elliptic SF$_6$ gas cylinder is the first to be considered before the calculations, as it may directly impact on cylinder instability evolution. According to the experimental initial image and the interfacial transition layer assumption, an approximate "diffused elliptic cylinder" initial condition of 2D diffuse interfacial transition layer with finite thickness is constructed. The SF$_6$ gas density is calculated by 2D Gaussian function:

$$\rho(\alpha_k,\beta_k) = \chi_0 \rho_{SF_6} e^{-[(\alpha_k - \alpha_{\min})^2 + (\beta_k - \beta_{\min})^2]/\delta^2}, \quad (3)$$

$$(x - x_0)/\alpha_k^2 + (y - y_0)/\beta_k^2 < 1, \quad k = 1, M. \quad (4)$$

where $x_0=y_0=0$, $\alpha_k \square [\alpha_{\min}, \alpha_{\max}]$, $\beta_k \in [\beta_{\min}, \beta_{\max}]$, $\alpha_{\min}=\beta_{\min}=1.0 \times 10^{-5}$ mm, $\alpha_{\max}$=6.30 mm, $\beta_{\max}$=2.30 mm, $\alpha_k=\alpha_{\min}+(k-1)d\alpha$, $\beta_k=\beta_{\min}+(k-1)d\beta$, $d\alpha=(\alpha_{\max}-\alpha_{\min})/M$, $d\beta=(\beta_{\max}-\beta_{\min})/M$, M=1000, and δ=6.16 mm. χ_0 is the concentration at the elliptic center, χ_0=0.71 in the elliptic case. The initial density image and distributions along major and minor axes of the ellipse are plotted in Fig. 2 (b). The difference in the SF$_6$ gas concentrations at the center of the two kinds of gas cylinders leads to a certain difference in the initial density peaks and distributions between the circular and elliptic gas cylinders. In the circular case, a core with definite size radius could exist where the density is uniformly distributed. Although the idea of the elliptic initial density comes from the circular case, but under the cylindrical contoured nozzle with ellipse size 2.5 mm $\times$ 10.0 mm and 2D diffuse effects, in our elliptic SF$_6$ gas cylinder experiment, not only the density peak is reduced, but also the core may be absent in the symmetrical center of the cylinder.
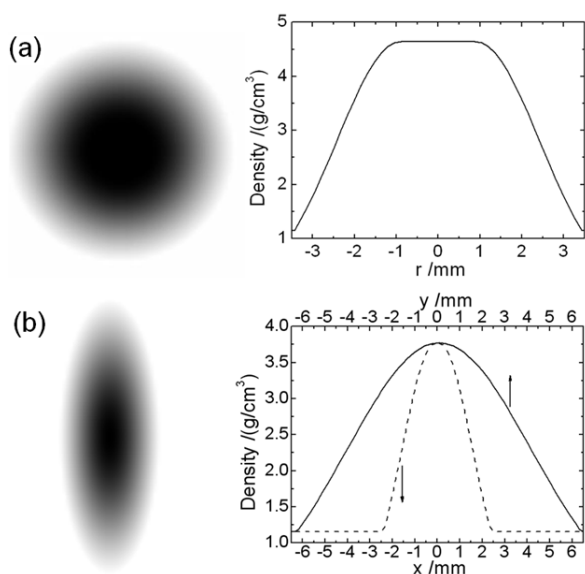

Fig. 2 The density images and distributions of the (a) circular and (b)

elliptic SF$_6$ gas cylinder initially constructed. (The sizes of the images are same as Fig. 1)

Due to the symmetry of the gas cylinder and model, the calculating region [-2.0 cm, 18 cm]×[0.0 cm, 2.5 cm] is adopted, which is the upper half of the whole one [-2.0 cm, 18 cm]×[-2.5 cm, 2.5 cm], and it is discretized into 2500 × 312 grids. Sample images from the 2D numerical results are shown in Fig. 1 (b), (d), and (f). These images have been chosen because they can illustrate some salient features of the experiments. From the Fig 1 (a) and (b), (c) and (d), (e) and (f), we can see that good qualitative agreement was achieved between the images obtained from the simulations and the experiments. Quantitative measurements allow us to perform a more rigorous comparison that can be made on the basis of a visual inspection of evolutionary images. In the three experiments, we mainly compared the length measurements of the evolving cylinders at each experimental time. The width and height of the evolving cylinders are measured using the six experimental and computational images. To distinguish the three experiments with three kinds of initial contoured nozzle, we use the shapes of these three kinds of initial contoured nozzles to denote them in our simulations respectively. We define the width as the horizontal length or the streamwise dimension of the evolving cylinder, and likewise the height as the vertical length or the spanwise dimension of the evolving cylinder, the same as in literature [17]. Plots of the width and height are shown in Fig. 3. We can see that quantitative agreements were achieved between the experimental and computational width and height of the evolving cylinders. Because of the errors in measuring the interface positions between air and diffused SF$_6$ gas from the experiment initial images, the initial width and height in our simulations are slightly greater than those in the experimental. Actually, the experimental and computational initial conditions were important for the width and height values, and the initial state of the elliptic is more sensitive and more inenarrable than the circular.

In the two vertical shock-accelerated directions to the elliptic heavy gas cylinder experiments, a large difference existed from the experiment images at the same times in Figure 1 (c) and Figure 1 (e), and a conclusion was easily obtained, that the second experiment has more stronger convergence than the third experiment. To illuminate this phenomenon from the simulations, we mainly analyze the vorticity, the circulation of each vortex and the distance between the two vortex cores. In the MVFT code, vorticity is determined by calculating the curl of the velocity field. This relationship for the 2D flow is:

$$\omega(x,y,t) = \nabla \times \mathbf{V} = \partial v/\partial x - \partial u/\partial y, \quad (5)$$

where $\mathbf{V}$ is the 2D velocity vector, and u and v are the x and y components of the velocity. Circulation is a measure of the average vorticity over an area A,

$$\Gamma(t) = \int_A \omega(x,y,t) \cdot dA. \quad (6)$$

World Academy of Science, Engineering and Technology
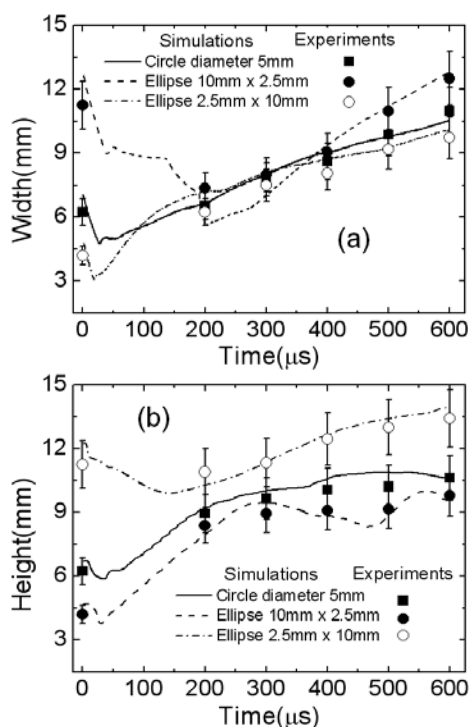International Journal of Physical and Mathematical Sciences
Vol:5, No:4, 2011

Fig. 3 Comparison of the width and height between the experiments and simulations. (The error bars of this visual measurement are equal to $\pm$ 10%)

In our experiments, the elliptic heavy gas cylinder evolves into a vortex pair due to the deposition of vorticity on the cylinder interface, and two obvious vortex cores are formed in the flow field. The vorticity has a negative maximum value in the vortex core of the upper half region we concerned, and it has a positive maximum value in the vortex core of the lower half region. Here, we use a parameter d to describe the distance between the two vortex cores. Figure 4 shows the vorticity at the center of the core and the distance between the two vortex cores of these two simulations. We can see the evident difference between the two cases: the initial contoured nozzle of 10.0mm × 2.5mm model has larger absolute values of $|\omega_{core}|$ at the center of the vortex cores than the 2.5mm × 10.0mm model at the same times, with an average discrepancy factor of about 1.72 during the time 600 μs; the former has smaller ds than the latter, with an average discrepancy factor of about 0.61. Because of this, it appears the 10.0mm × 2.5mm model has a stronger effect of convergence than the 2.5mm × 10.0mm model. In our calculation, the gas jet appears at the symmetry center of cylinder during the early times, shown in Fig. 1 (d). This difference was due to the shock wave loading elliptic heavy gas cylinder in different major axis direction. Moreover, the results of verification can also be calculated by circulation. Figure 5 shows the positive circulation, the negative circulation and the total circulation evolution over time of the flow field. From the Figure 5, it is clear that, although the two models differ little in the positive circulation, the difference is more obvious in the negative circulation, resulting in the great difference in the total

circulation of the flow field. The absolute value of the former is larger than the latter, consistent with the results of the vorticity of the vortex cores. This phenomenon reveals new features that previously studied circular cylinders do not have.
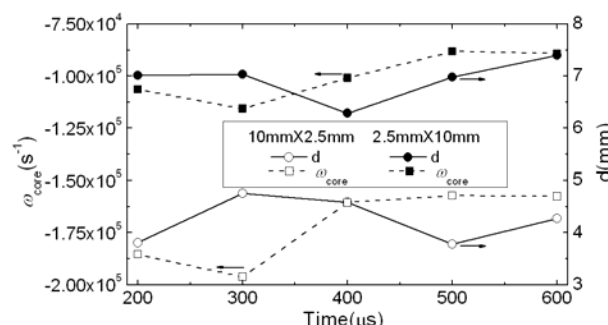

Fig. 4 The vorticity at the center of the core and the distance between the two vortex cores of these two simulations
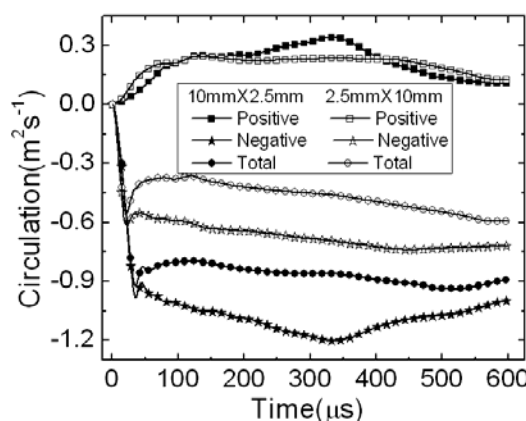

Fig. 5 The positive circulation, the negative circulation and the total circulation evolution over time of the flow field of the two elliptic gas cylinders

V. CONCLUSIONS

In summary, based on the circular gas cylinder experiment and simulations, we studied the evolution of elliptic heavy SF_6 gas cylinders surrounded by air when accelerated by planar shocks. The relationship between the elliptic and circular gas cylinders is constructed by an approximate initial condition of 2D diffuse ITL with finite thickness. By using a multiple dynamics imaging technology, the experiment initial conditions and five images of the time evolution of circular and elliptic cylinders were obtained. With the help of our numerical simulation tool, we compared the width and height of the circular and two kinds of elliptic gas cylinders, and analyzed the effect of convergence and vortex features of the induced gas cylinder with time under the different shock-accelerated direction to the elliptic gas cylinder. But due to the different initial gas cylinder shapes, a certain difference of the initial density peak and distribution existed between the circular and elliptic gas cylinder. In this investigation, although we succeeded to build a possible link between the gas columns, the elliptic ones are more complicated and hard to describe objective reality. Actually, it's difficult to be imagined for the

World Academy of Science, Engineering and Technology
International Journal of Physical and Mathematical Sciences
Vol:5, No:4, 2011

more complex initial gas cylinder shapes.

REFERENCES

[1] J. W. Grove, R. Holmes, D. H. Sharp, Y. Yang, and Q. Zhang, "Quantitative theory of Richtmyer-Meshkov instability," *Phys. Rev. Lett.*, vol. 71, pp. 3473–3476, Nov. 1993.

[2] K. O. Mikaelian, "Growth rate of the Richtmyer-Meshkov instability at shocked interfaces," *Phys. Rev. Lett.*, vol. 71, pp. 2903–2906, Nov. 1993.

[3] D. Hill, C. Pantano, and D. Pullin, "Large-eddy simulation and multiscale modelling of a Richtmyer–Meshkov instability with reshock," *J. Fluid Mech.*, vol. 557, pp. 29–61, Jun. 2006.

[4] K. O. Mikaelian, "Analytic Approach to Nonlinear Rayleigh-Taylor and Richtmyer-Meshkov Instabilities," *Phys. Rev. Lett.*, vol. 80, pp. 508–511, Jan. 1998.

[5] S. Gupta, S Zhang, and N. J. Zabusky, "Shock interaction with a heavy gas cylinder: Emergence of vortex bilayers and vortex-accelerated baroclinic circulation generation," *Laser and Particle Beams*, vol. 21, pp. 443–448, Apr. 2003.

[6] K. Prestridge, P. Vorobieff, P. Rightley, and R. F. Benjamin, "Validation of an Instability Growth Model Using Particle Image Velocimetry Measurements," *Phys. Rev. Lett.*, vol. 84, pp. 4353–4356, May 2000.

[7] N. J. Zabusky, and S. Zhang, "Shock–planar curtain interactions in two dimensions: Emergence of vortex double layers, vortex projectiles, and decaying stratified turbulence," *Phys. Fluids*, vol. 14, pp. 419–422, 2002.

[8] C. Tomkins, K. Prestridge, P. Rightley, and M. Marry-Lyon, "A quantitative study of the interaction of two Richtmyer–Meshkov-unstable gas cylinders," *Phys. Fluids*, vol. 15, pp. 986–1004, Mar. 2003.

[9] S. Kumar, P. Vorobieff, G. Orlice, A. Palekar, C. Tomkins, C. Goodenough, M. Marry-Lyon, K. Prestridge, and R. F. Benjamin, "Complex flow morphologies in shock-accelerated gaseous flows," *Physica D*, vol. 235, pp. 21–28, Nov. 2007.

[10] G. Layes, C. Mariani, G. Jourdan, L. Houas, F. Renaud, and D. Souffland, "Experimental observations of the reflected shock effect on an accelerated gas bubble interface," in *Proc. 10th Int. Workshop on the Physics of Compressible Turbulent Mixing*, Paris, 2006.

[11] P. B. Puranik, J. G. Oakley, M. H. Anderson, and R. Bonazza, "Experimental study of the Richtmyer-Meshkov instability induced by a Mach 3 shock wave," *Shock Waves*, vol. 13, pp. 413–429, Jun. 2004.

[12] E. Meshkov, "Instability of the interface of two gases accelerated by a shock wave," *Fluid Dyn.*, vol. 4, pp. 101–104, 1972.

[13] J. S. Bai, J. H. Liu, and T. Wang, L. Y. Zou, P. Li, and D. W. Tan, "Investigation of the Richtmyer-Meshkov instability with double perturbation interface in nonuniform flows," *Phys. Rev. E*, vol. 81, pp. 056302, May 2010.

[14] P. Colella and P. R. Woodward, "The piecewise parabolic method (PPM) for gas-dynamical simulations," *J. Comput. Phys.*, vol. 54, pp. 174–201, 1984.

[15] W. Vreman, "An eddy-viscosity subgrid-scale model for turbulent shear flow: Algebraic theory and applications," *Phys. Fluids*, vol. 16, pp. 3670–3681, Sep. 2004.

[16] J. S. Bai, T. Wang, P. Li, L. Y. Zou, and D. W. Tan, "Numerical analyse of the turbulence mixing of re-shocks with a perturbation interface," *Sci. China Ser. G*, vol. 39, pp. 1646–1653, Nov. 2009.

[17] C. A. Zoldi, in *Applied Mathematics and Statistics, State University of New York at Stony Brook*, Doctor Dissertation, 2002.